

Learning-based Damage Recovery for Healable Soft Electronic Skins

Seppe Terryn^{†}, David Hardman[†], Thomas George Thuruthel, Ellen Roels, Fatemeh Sahraeeazartamar and Fumiya Iida*

^{*}E-mail: seppe.terryn@vub.be

[†]These authors contributed equally to this work.

S. Terryn and E. Roels

Brubotics, Vrije Universiteit Brussel (VUB) and Imec; Pleinlaan 2, 1050 Brussels, Belgium.

S. Terryn, David Hardman, Thomas George Thuruthel and Fumiya Iida

Bio-Inspired Robotics Lab, University of Cambridge; Trumpington Street, Cambridge, CB2 1PZ, United Kingdom.

F. Sahraeeazartamar

Physical Chemistry and Polymer Science (FYSC), Vrije Universiteit Brussel (VUB);
Pleinlaan 2, 1050 Brussels, Belgium

Keywords: machine learning, electronic skins, self-healing, transfer learning, damage recovery, flexible electronics, soft sensors.

Natural agents display various adaptation strategies to damages, including damage assessment, localization, healing, and recalibration. This work investigates strategies by which a soft electronic skin can similarly preserve its sensitivity after multiple damages, combining material-level healing with software-level adaptation. Being manufactured entirely from self-healing Diels-Alder matrix and composite fibers, the skin is capable of physically recovering from macroscopic damages. However, the simultaneous shifts in sensor fiber signals cannot be modelled using analytical approaches, since the materials viscoelasticity and healing processes introduce significant nonlinearities and time-variance into the skin's response. We show that machine learning of 5-layer networks after 5000 probes leads to highly sensitive models for touch localization with 2.3mm position and 95% depth accuracy. Through health monitoring via probing, damage and partial recovery are localized. Although healing is often successful, insufficient recontact leads to limited recovery or complete loss of a fiber. In these cases,

complete resampling and retraining recovers the networks' full performance, regaining sensitivity and further increasing the system's robustness. Transfer learning with a single frozen layer provides the ability to rapidly adapt with fewer than 200 probes.

1. Introduction

Soft sensors made of highly deformable materials are one of the enabling technologies in developing a number of soft robotic systems^[1] and wearable devices.^[2–4] They are typically used to measure contact, deformation, pressure, and stress information based on an electrical response to a mechanical stimulus. Sensing mechanisms include conductive liquids,^[5] elastomeric composites with conductive fillers,^[6] ionic hydrogels,^[7] and optical fibers.^[6,8] As these sensors are designed to undergo large deformations over repeated cycles, they are susceptible to fatigue and degradation over time, and are easily damaged by sharp objects. Using self-healing functional materials can therefore improve the reliability, stability, and long-term performance of these soft sensors.^[9–12]

Recently, there has been increasing interest in the development of self-healing materials for soft robotic applications.^[13] Self-healing polymers can be used for structural support,^[14] as functional soft actuators^[15,16] or as electronic components.^[10,12] Self-healing electronic devices can range in complexity from conducting wires,^[17] to semiconductors & dielectric materials^[18,19] and to sensing elements.^[20–23]

One of the earliest works on a self-healing sensor used a piezo-resistive composite made of μNi particles and a self-healing polymeric material.^[21] Similarly, piezo-resistive composites with better electrical properties were developed using different functional conductive materials.^[24,25] These sensors change their electrical properties in response to a strain signal and can hence be used for proprioception, force estimation and contact localization. Hardman et al. use the piezoresistive response of an ionic gelatin/glycerol hydrogel to develop self-healing soft strain sensors for pneumatic actuators.^[26] Contact localization and force sensing can also be done with soft self-healing capacitive sensors.^[27] Capacitive sensing technologies, however, require more involved electronic hardware and suffer from parasitic capacitive effects. Other types of self-healing sensors include temperature sensors,^[28] chemical sensors,^[29] and damage detection sensors.^[30] All demonstrate the recovery of electrical properties after damage, but have not investigated the modelling of these sensors and the functional integrity of these models after a damage-heal cycle.

Soft robotic sensors present numerous challenges in their modelling. This is because they tend to be responsive to multiple physical cues, exhibit temporal nonlinearities (hysteresis & drift), and their properties are linked to the surrounding matrix.^[2] As extensively demonstrated in this work, these undesired dynamic effects are particularly present in healable soft sensors since they are manufactured out of dynamic reversible polymers and have a viscoelastic behavior. In addition, partial recoveries after healing lead to new sensor behaviors, requiring recalibration. Hence, learning-based approaches, which are becoming increasingly popular in sensor modelling,^[31,32] can be the enabling technology for healable soft sensors. Deep learning techniques have shown promise for modelling these time-variant sensor properties.^[33,34] Long-short term memory networks are typically used to capture drift and hysteresis in the sensors. However, these dynamic networks require a continuous stream of sensor data at a fixed sample rate for state estimation, making them challenging for practical applications. Alternatively, static networks can be used with explicit sensor history^[35] or redundant sensor configuration.^[36] In this work, we use deep static networks for drift and hysteresis compensation. In addition, these learning-based approaches are used to model multi-sensor electronic skins,^[32] multi-electrode piezoresistive sensors^[37] and electrical impedance tomography (EIT) sensors,^[38] having a complex relationship between their resistances/impedances and location of touch. Although machine learning has its sampling and training cost, it allows to make high performance electronic skins out of extremely inexpensive conductive polymer composite sheets^[39,40] or carbon electrode fibers,^[41] reducing hardware costs.

We present a deep-learning approach for the modelling of a self-healing skin, composed of eight resistive strain sensors, enabling contact localization and depth perception. Although the presented approach is applicable to a wide variety of self-healing materials and sensor morphologies, a general grid-based sensor morphology is selected, composed of a Diels-Alder polymer matrix and conductive Diels-Alder composite fibers. We show how temporal nonlinearities in the sensor response can be compensated using response history and deep neural networks to provide highly accurate state estimation models. Methods for health monitoring, damage detection, and damage localization are presented. As the healed sensors undergo behavioral transformations, we show that transfer learning techniques can be used to recover functionality, enabling the model to be accurately updated with minimal resampling. Our work is the first demonstration of a complete framework for adapting to damages in a soft bodied system, covering damage detection, localization, healing, and recalibration of internal models.

2. Results

2.1. Design of the Healable Artificial Skin

In this work, a completely healable soft electronic skin is created composed of an insulating self-healing 55x55x5 mm³ square matrix (**Figure 1A**, yellow), in which eight conductive fibers (**Figure 1A**, black) are integrated in a grid based morphology. These fibers function as resistive strain sensors and have a diameter of 0.5 mm. The healing of both the polymer matrix and composite fibers are relying on Diels-Alder crosslinks in the polymer/composite network, discussed in the following Section 2.2. Four fibers are embedded straight in the x-directions with a distance of 11 mm between them and at a depth of 2.5 mm. The other fibers are embedded perpendicular to these, in the y-direction, also with a distance of 11 mm between them, but at a depth of 3.5 mm. Consequently, perpendicular fibres do not touch in the matrix. Both the matrix and fiber material are flexible, and consequently the skin acts as a soft sensor network that is bendable and stretchable and can potentially be used in soft robotics, including embedding touch sensing in soft grippers (**Figure 1A**). Additionally, since both materials are self-healing, the entire electronic skin can be healed.

2.2. Artificial Healing on the Material Level

Finding inspiration in biology, scientists have been developing synthetic materials possessing biomimetic healing abilities.^[42] Many are polymer networks relying on reversible (physico) chemical crosslinks, like the equilibrium Diels-Alder reaction between a furan and maleimide (blue and red in **Figure 1B**).^[43] Two different Diels-Alder polymer networks are synthesized; the non-conductive BMI1400-FT3000-r0.5 material used as matrix and the conductive DPBM-FT5000-r0.6-20 wt%CB260 composite used for the fibers (details in Materials and Methods). As these polymers contain the reversible Diels-Alder crosslinks, they can both heal. When cuts are made, the Diels-Alder bonds locally break, generating reactive maleimide and furan on the fracture surfaces (**Figure 1C**). However, being reversible, these covalent bonds can be reformed when bringing the fracture surfaces and reactive maleimide and furan groups back together. Upon excellent contact and limited misalignment of the fracture surfaces, healing can occur even at room temperature.^[44] Nevertheless, microscopic gaps caused by misalignment or imperfect contact can be sealed by heating at a higher temperature (90°C) which increases mobility in the polymer network.

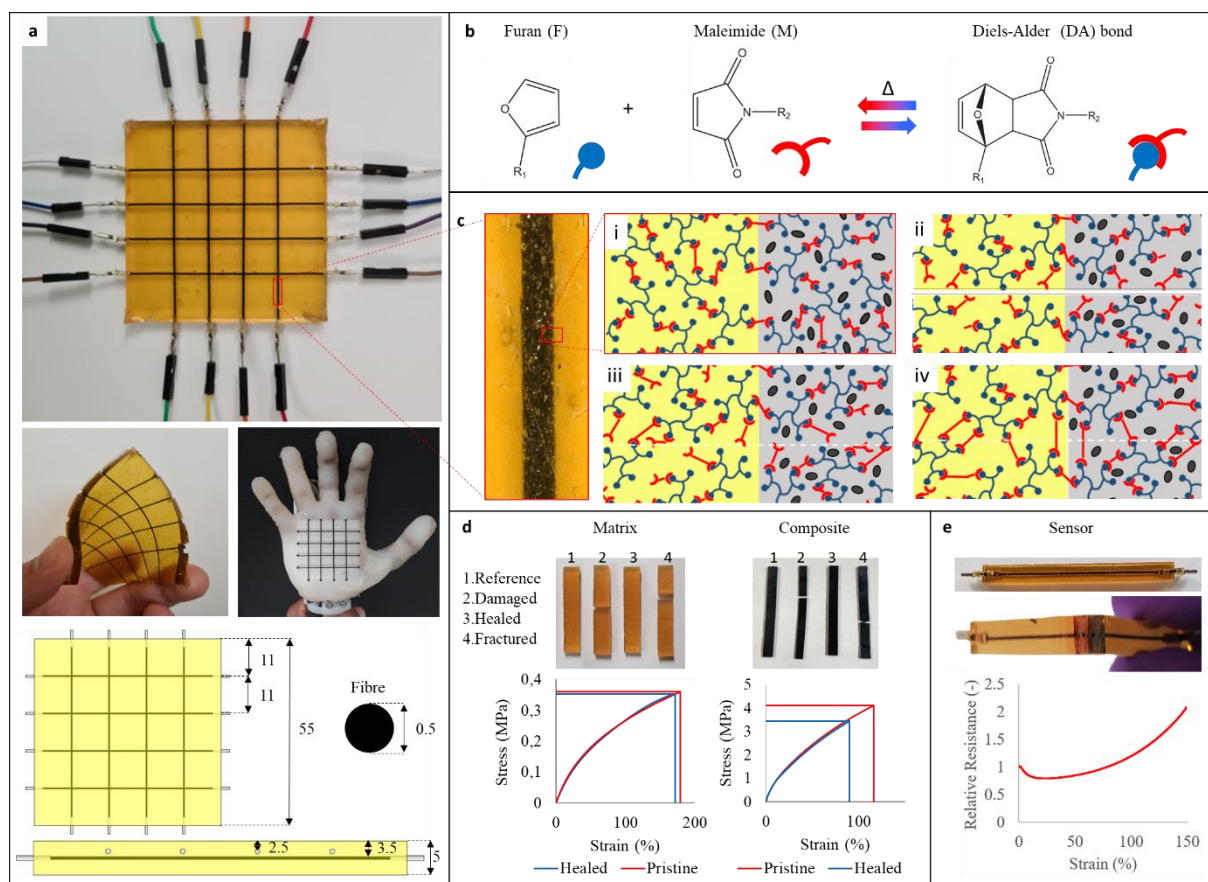


Figure 1. (A) The equilibrium reaction between maleimide (red) and furan (blue) forms a reversible Diels-Alder bond. (B) The self-healing artificial skin, composed of a sensor network with a grid-based sensor morphology. Eight flexible and healable strain sensors are embedded in the healable matrix. The entire artificial skin is flexible. (C) The fiber has a diameter of 0.5 mm and is made from an elastomer that is crosslinked via reversible Diels-Alder-bonds and is filled with carbon particles, making it conductive. This fiber is embedded in a Diels-Alder matrix. As both the fibers and the matrix are made from Diels-Alder elastomers, the interface between fiber and matrix is covalently bonded, leading to a high interfacial strength enhancing the sensor performance. (D) Both the conductive Diels-Alder composite and non-conductive Diels-Alder matrix are healable due to the presence of reversible Diels-Alder crosslinks in their polymer network, as illustrated by recovery of the mechanical properties in a tensile stress strain test with strain ramp of $1\%s^{-1}$, after being cut completely in half, brought back in contact and healed for 1 hour at $90^{\circ}C$. (E) The resistance-strain relationship, obtained from a tensile test on a single strain sensor ($55 \times 10 \times 1 \text{ mm}^3$) with a strain ramp of $1\%s^{-1}$, is non-linear and is a surjection for the entire strain window. In addition, the loading and unloading curves form a hysteresis loop.

This remarkable healing capacity can be illustrated via tensile testing (**Figure 1D**), as well as the stretchability of this Diels-Alder polymer and composite, shown by fracture strains surpassing 100%. Samples are cut in half using a scalpel blade, brought back in contact and healed by heating to 90°C for 1 hour. When fracturing these healed samples in the tensile test and comparing them to a pristine (undamaged) sample, it is clear that the mechanical properties are recovered after this healing process (**Figure 1D**). For the polymer (yellow), the fracture stress is recovered with a high healing efficiency of 98%, and fracture not initiating at the healed site. Although the mechanical behavior of the composite (black) is recovered for strains below 90%, the fracture stress is not completely recovered and a healing efficiency of 81% is measured (**Figure 1D**). In addition, the baseline resistance changed from 285 Ohm to 460 Ohm, recovering the electrical properties with 60% efficiency. This reduction in healing capacity results from the carbon black C260 fillers, which provide conductivity, but reduce the mobility in the polymer network. Nevertheless, a recovery of the mechanical behavior until strains of 90% provides sufficient recovery for many applications, such as healable soft sensors^[10] and embedded heaters for soft robotics or smart wearable devices.^[45]

2.3. Response of the Healable Artificial Skin

Initial tests are performed using a 55x10x2 mm³ sensor consisting of a conductive DPBM-FT5000-r0.6-20wt%CB260 fiber with a 0.5 mm diameter that is embedded in an insulating BMI1400-FT3000-r0.5 (**Figure 1E**). Being constructed solely out of self-healing polymers this entire resistive strain sensor is healable and can even recover from being cut in half, subjecting it to a temperature of 90°C for one hour. Upon stretching in a tensile test with fixed strain ramp of 0.01s⁻¹, the resistance presents a complex surjective relationship with a non-unique mapping between resistance and strain,^[46] which is challenging to express analytically.

Resistive strain sensors based on conductive elastomeric nanocomposites are not only hard to model due to their high nonlinearity (**Figure 1E**), but also due to their time dependent stress/resistive-strain responses caused by the viscoelastic nature of the elastomeric matrix. These effects can be seen in the responses of the skin's eight sensor fibers when pressed and held at three different locations using a robotic probe (**Figure 2A**). Conversely, **Figure 2B** shows the skin's repeated response when pressed and held at a single location at a depth of 1.5 mm. As the probe moves with a speed of 7 mm s⁻¹ and the probing depth is only 1.5 mm, it is clear that the sensor response is time dependent, indicated by the elastic recovery time of up to 3 seconds upon release. The relationship between the probing location in the *x-y* plane (dark

orange zone indicated in **Figure 2A**), the depth and the sensor response is not easy to model, as already evident by the non-linear response of the sensor to strain (**Figure 1E**). This can be seen by the skin's response to probing at three different locations at varying depths (**Figure 2B**). Depending on the amount of deformation and its location, the sensor resistance can either increase or decrease, more than two sensors can be activated to a single contact, and the sensors may not return to their initial conditions after probing (due to hysteresis and drift).

Healing of a damage can lead to non-complete recovery of the mechanical properties (**Figure 1D**), but also of the sensor performance. In a third test in **Figure 2B**, the artificial skin is tested by probing with a depth of 1.5 mm at a single location prior to damage, after damage and after being healed. Damage is induced using a scalpel blade and slicing completely through one of the sensor fibers. Looking at **Figure 2B**'s sensor response after damage, it can be seen that the damaged fiber regains electrical contact autonomously after the blade is retracted. This is due to self-sealing, which results from the elastic recovery of the matrix. However, upon probing, the cut reopens leading to a spike to high voltage in the sensor response, indicating that the sensor is still damaged. After healing, the sensor property is regained. However, its response is clearly different from before damage.

It is important to note that the baseline resistances of the undamaged fiber sensors also change after healing. This is probably caused by a slight reconfiguration of the carbon particles/agglomerates in the composite, or by increased contact between the fiber and the crimp connector. Both are induced by a high polymer network mobility, caused by the increase in temperature during the healing process. Due to the influence of healing on the baseline of the sensors, recalibration is necessary in order to preserve the sensitivity of the artificial skin. Altogether, the effects described in this section make the modelling of these healable artificial skin challenging, especially using analytical methods.

2.4. Machine-Learning for Contact Localization

The challenges described in previous sections can be circumvented by generating data-driven models of the healable electronic skin. There are two considerations to be made in the design of the learning architecture. First, the network should be able to compensate for the non-linearities in the sensor response, particularly the ones caused by drift and hysteresis. This is done by appending the inputs to the network with the sensor-response history. Second, the network should be easy and quick to adapt to repeated damage-and-healing cycles. This can be achieved with a sufficiently deep network and transfer learning techniques.^[47]

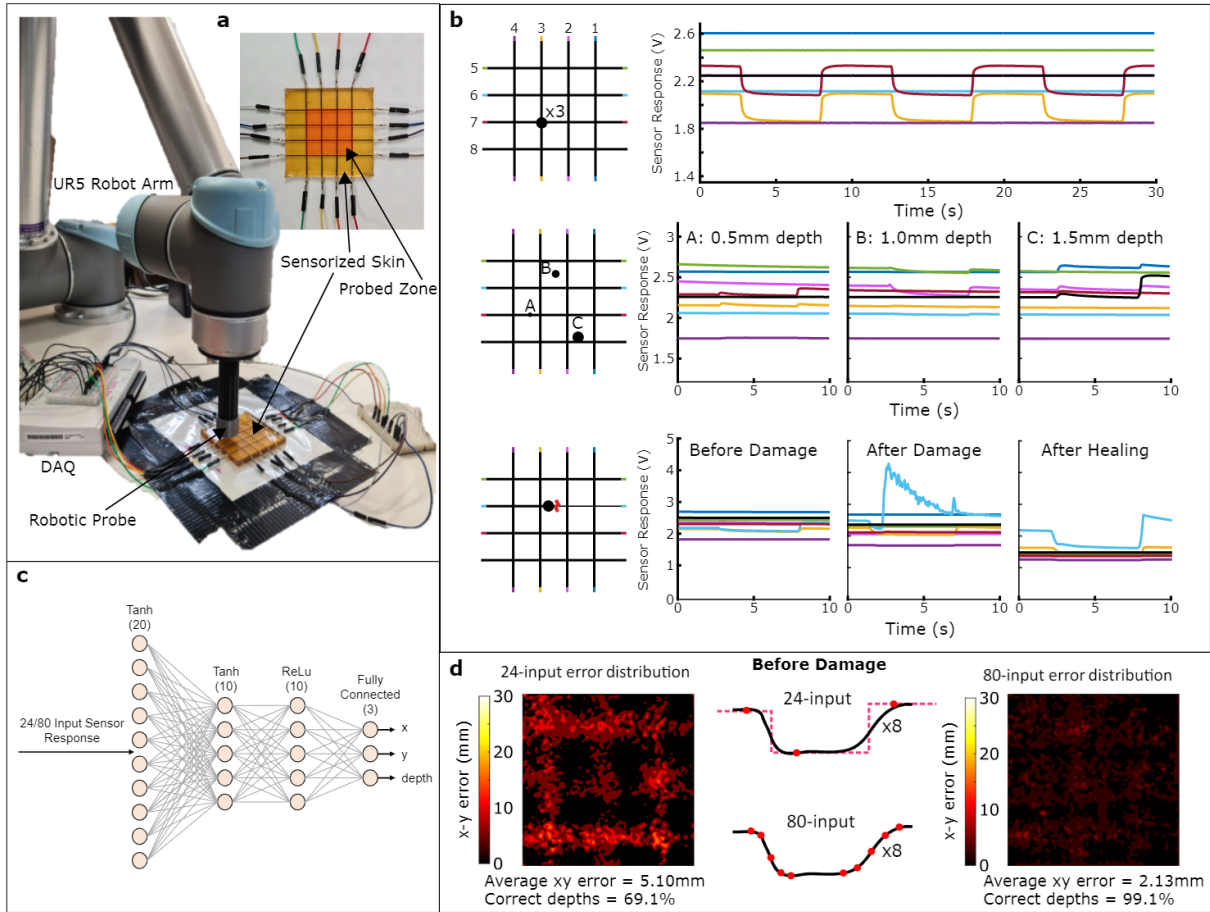


Figure 2: (A) The training setup, consisting of a UR5 manipulator from Universal Robots equipped with a cylindrical end effector probe with a diameter of 5 mm. The UR5 probes the soft sensor matrix at different locations within the red zone indicated on the sensor matrix with a depth of 0.5 mm, 1 mm or 1.5 mm in order to evaluate the skin's sensitivity. (B) The raw signals from the eight sensors while pressing at the location indicated by a black dot on the sensor matrix. i shows the repeatability of the response to three identical presses. In ii, 3 locations are probed, each at a different depth. iii plots the response to a probe directly next to a damaged area before and after damage and healing. (C) The architecture of the deep neural network used throughout this work to map the sensor responses to the predicted x - y location and depth of probing. The size of the input layer can be varied, with the architecture of the output and 3 hidden layers remains fixed. (D) Comparisons of the 24-input and 80-input network performances when trained on 4500 probes of the undamaged skin. The 24-input case first fits a representative square wave to each of the 8 sensor's responses, sampling the three marked locations for the network's input. The 80-input case uses no signal filtering, and instead directly samples 10 points from each sensor during the press and release of the probe. The x - y error distributions (predicted vs actual) over (A)'s zone are plotted, and the proportion of depths correctly guessed is calculated. The 80-input method is chosen for further use: additional input numbers are tested in Figure S1.

Figure 2C's network architecture can take either 24 or 80 inputs to predict the location & depth of skin contact, corresponding to either 3 or 10 samples from each of the 8 sensor responses on specific times (see Materials and Methods and Figure S2). When 3 samples are taken, the signal response is first fitted to a square wave, with samples taken before, during, and after contact. **Figure 2D** shows the x - y error magnitude of a network trained on 4500 probes of the undamaged skin, each randomly located and with 0.5, 1.0, or 1.5 mm depth inside the red square (**Figure 2A**). Uncertainties caused by symmetries in the major sensor responses are visible as a grid of higher errors,^[35] leading to an average error of 5.10 mm for the x - y probing position, and the correct depth being identified 69.1% of the time. Contrastingly, the network trained with 10 samples from each sensor (**Figure 2D**) shows a much more uniform and low error of only 2.13 mm, whilst correctly identifying >99% of the probed depths. The training and validation datasets perform extremely similarly (Figure S3), suggesting that this is not merely a result of overfitting to the test data. The 80-input architecture is selected for further experimentation; as well as lower-error predictions, the samples do not require a square wave to be fitted to the data, and are simply sampled from the raw voltage measurements.

2.5. Damage Types

In this work, we distinguish three types of damage inside the healable artificial skin. All these damages result from cutting through a single sensor fiber and the surrounding matrix using a scalpel blade (**Figure 3A**). However, the three differ in the recovery of the system from this damage. (i) In the first case, the sensor fiber regains electrical contact almost immediately after retracting the blade (Movie S2), due to a very clean damage, excellent elastic recovery of the sensor matrix and negligible misalignment. As a result of excellent contact, the healing takes place instantaneously at room temperature, as described in a previous work.^[44] For this autonomous healing, it is important that contact is regained instantaneously after damage, when the number of reactive maleimide and furan compounds is still high. (ii) In the second case, recontact is not achieved immediately, but after some time (Movie S5) due to slower elastic recovery. During this time, the available reactive maleimide and furan react with one another on separate fracture surfaces. Consequently, healing at the damaged surface is slowed down considerably, e.g. in the order of hours, at room temperature. Nevertheless, this damage can be healed by heating the artificial skin to 90°C for 1 hour. (iii) Lastly, in some damage cases, contact is not initially regained. However, upon heating of the artificial skin, an increase in molecular mobility and thermal expansion of the matrix and fibers causes recontact. After recontact, this damage heals during the heating process.

2.6. Health Monitoring, Damage Detection and Localization

Damages in the artificial skin can be detected by monitoring the resistance of the eight sensors. Upon cutting one of the sensors using a scalpel blade (**Figure 3A**), its measured resistance becomes infinite and the voltage across the resistor jumps to 5 V. This is done for three damages in two of the eight sensor fibers (**Figure 3B-D**). By detecting this sharp increase in voltage, the system can easily isolate the damaged sensor line. After the blade is retracted, further tracking of the sensor response allows the detection of recontact due to self-sealing, caused by the elastic recovery of the matrix. This recontact can appear immediately after damage (**Figure 3B**), in which case the initial sensor state is reached after the blade is retracted. Alternatively, recontact can also be achieved when the skin is touched close to or on the damaged location (**Figure 3C**). To narrow down the location of damage, the UR5 manipulator probes 100 equally-spaced points along the damaged fiber with increments of 0.3 mm, while tracking the sensor signal for voltage spikes (**Figure 3B**). At each location, the difference in voltage during probing and directly before/after probing is calculated and plotted, i.e.

$$\Delta V = \left(\frac{V_{before} + V_{after}}{2} \right) - V_{during} \quad (1)$$

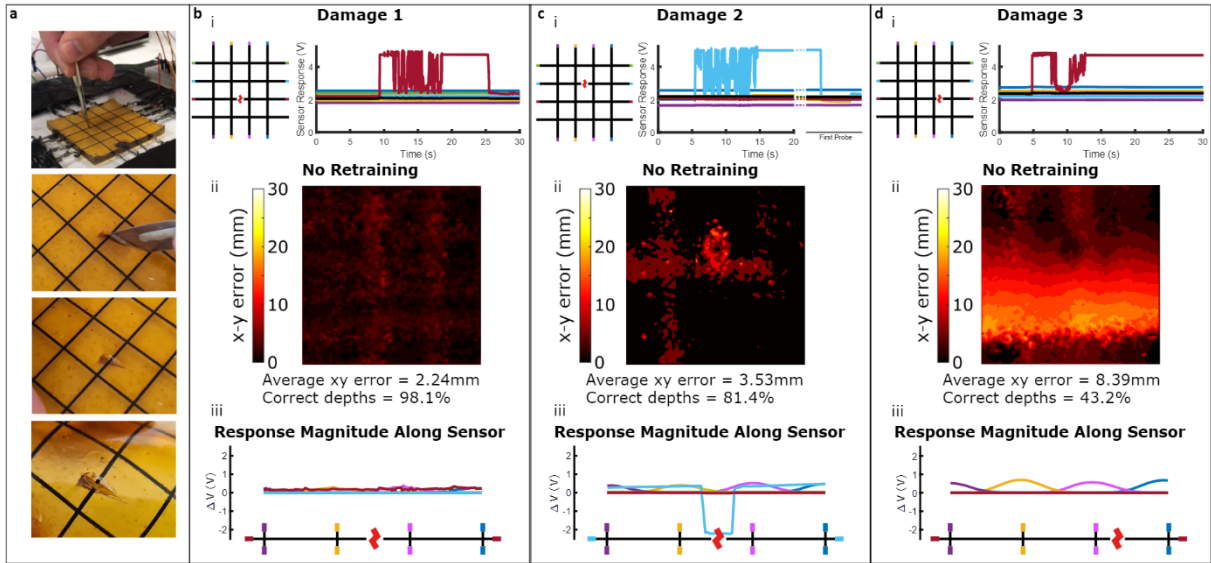


Figure 3: Damage and damage detection in the electronic skin for three damage cases. For each, the damage locations are marked on a representative grid, and the sensor responses to cutting are plotted (see Movie S2). After damage, 5000 new points are probed (see **Figure 2**), used to evaluate the performance of a network trained on the skin's behavior before each damage. In addition, in iii, 100 probes are measured along the damaged sensor, and $\Delta V = \left(\frac{V_{before} + V_{after}}{2} \right) - V_{during}$ is calculated at each point for the eight sensors. **(A)** The damages are clean scalpel cuts through the matrix and sensor. **(B)** Damage 1: The sensor is cut, but immediately regains and maintains contact when the scalpel is removed. **(C)** Damage 2: Contact is partially regained shortly after damage - during the first probe -

but the sensor still separates and loses the electrical connection when probed close to the damaged area.

(D) Damage 3: Contact is not regained, and the damaged sensor shows no response.

For the first damage, contact is regained immediately and, looking at ΔV along the fiber, it can be seen that the fiber maintains electrical contact, returning a small and relatively constant reading at every location. This measurement suggests that the artificial skin is healed from this damage without the need for a healing procedure that involves heating. For the second damage (**Figure 3C**), probing along the damaged fiber shows that electrical contact is quickly regained, as the sensor is again sensitive. However, when probing near the damaged region, a loss of electrical contact due to insufficient healing leads to a strong discontinuity in the response. Information from other sensors can also be utilized for localization; clear bumps are visible as the probe passes over sensors aligned with the y -axis. As such, this probing method allows the identification of the location of damage in the x - y direction. For the third damage (**Figure 3D**), electrical recontact is not regained after damage, nor during probing. ΔV is zero for the damaged (red) sensor during the entire probing experiments, and the damaged location cannot be further narrowed down.

Damage detection can also be performed by probing the entire x - y plane of the artificial skin. In a second experiment, the UR5 manipulator probes 5000 random x - y coordinates within the red square (**Figure 2A**), with each randomly allocated to a depth of 0.5, 1.0, or 1.5 mm. After sampling the sensor responses, the probing location and depth are predicted using a network trained prior to damage, in order to highlight the differences in response introduced by the damage. The x - y error is calculated by comparing the estimated probing coordinates to the actual x - y probing position. For the first damage (**Figure 3B**), only a small increase in error can be detected at the location of damage, illustrating that the sensor is healed without the need for a temperature treatment. For the second damage (**Figure 3C**), the damage is clearly detected as the area which causes loss of contact when probed, resulting in a region with high error. For the last damage (**Figure 3D**), the error is large along the entire length of the damaged fiber, as electrical contact is not regained. Although this second damage-detection experiment allows clear visualization of the damage in the x - y plane, probing along the damaged fibers is a much faster method to localize damage. Nevertheless, this extensive probing approach is useful if the damage event is not detected, e.g. when it occurs when the system is offline.

Although it is not always possible to detect the exact location of damage, it is important for the system to investigate in order to facilitate its recovery. In addition, in future applications,

including soft robots and smart wearables, tracking of the locations of damage provides important information about parts and locations that are prone to damage. The sensitivity of both touch and damage can be increased by integrating a larger number of sensor fibers into the artificial skin.

2.7. Healing and Retraining

Damages are healed by subjecting the entire artificial skin to a temperature of 90°C and leaving it for one day at 25°C. From visual inspection in **Figure 4A**, it can be seen that the damage in matrix and fibers are healed, leaving only a small scar due to misalignment in damages 2 and 3. ΔV along the healed sensors are plotted in **Figure 4B-D**, to be compared with those of **Figure 3**. The first damage case shows a reasonably constant response, with a small bump near the damaged area illustrating the residual effect on the sensor's resistance at this location. The constant value is different to that of **Figure 3B**, reflecting the shift in baseline resistance and responsive properties undergone by all sensors during the temperature treatments. Though the x - y coordinates of each probe can still be localized to within ~ 3 mm by the network trained on the undamaged sensor, these shifts in resistance cause the proportion of correctly predicted depths to severely drop after healing. This decrease in sensitivity illustrates the importance of health monitoring and damage detection after damage occurs. If the damage is self-sealed and healed at room temperature, the system should not be heated, as this decreases its sensor performance. This decision to continue operation without heating will depend on a thorough health monitoring. Still, given new inputs from the healed skin, the network can adapt to this new behavior - when a new network is fully retrained on the same healed data, 96.1% correct depth predictions are found to be possible (**Figure 4B**).

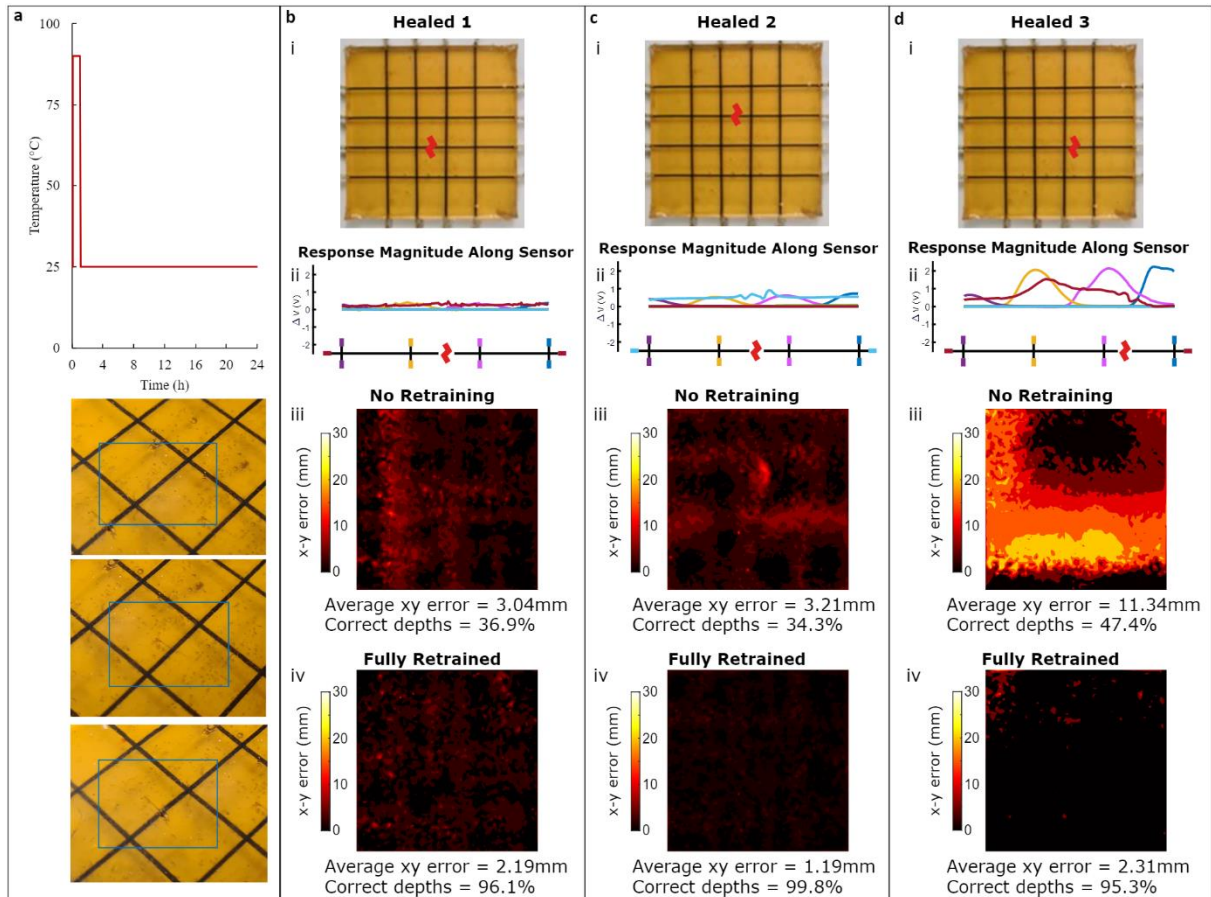


Figure 4: Healing and retraining of the electronic skin (A) The temperature-time profile during healing and images of the healed damages 1, 2 and 3. **(B-D)** Sensitivities of the damaged sensors (B-D in **Figure 3**) after healing of the three damage cases. In ii, the damaged sensors are probed along their lengths, whereupon the healing of case 2 is particularly clear when compared to the damaged plot. 5000 new points are probed after healing: first the x - y error distributions over the skin are shown for the networks trained before each damage (iii), and then compared (iv) to the errors of new networks trained using these 5000 data points with a 90:10% training:validation split. In all cases, full retraining results in better x - y localization and depth prediction.

In comparison with **Figure 3C**'s data, **Figure 4A**'s ΔV plot illustrates the significant improvement in response upon healing of the second damage case. The resistive effects of the damage are still visible (shown in blue), with a small instability in response appearing when the damaged area is probed. However, contact is now maintained throughout probing (Movie S4), with the response being much more constant along the entire fiber, and showing no significant discontinuity. The healing of this fiber is confirmed by **Figure 4C**'s sensitivity map before retraining, which shows clear improvement of the sensitivity at the damaged location. Compared to the pre-healed map, the average x - y error has increased, whilst the correct estimation of the depth has dropped to 34%. This is the result of a change in base resistance after the heat treatment, caused by a slight reconfiguration of the carbon particles/agglomerates

in the composite or/and changes in contact resistance at the interface of the fiber and the crimp connector. In order to adapt to this new sensory behavior, the pretrained network must undergo additional training to compensate for these new effects, to prevent the visibly damaged area seen in the error mapping of the 'no retraining' evaluation. Full retraining of a network with 4500 new data points from this healed skin is able to attain excellent x - y localization and depth prediction, outperforming even the undamaged network in **Figure 2D**.

Similarly, the third damage case, which previously showed no sensory response whatsoever, now responds nonlinearly to deformations of the skin (**Figure 4D**, red curve). However, for the final probing points the sensor response is small, indicating that contact is weak and the fiber is not properly healed. This is emphasized by the sensitivity map before retraining, in which the damage produces a large average localization error of 11 mm. However, a fully retrained network shows no such error, producing a uniform error distribution which performs comparably to the undamaged skin's network in **Figure 2D**. This illustrates the redundancy of the electronic skin towards individual sensor damage. This results from a redundancy of sensor fibers and the machine learning based calibration approach.

This redundancy is further emphasized in **Figure S2**, by the performance of a 70-input network trained, validated, and tested on the skin after the first damage case. For each, one of the eight sensors' data is entirely removed. The uniform sensitivity maps, < 2 mm localization, and $\sim 100\%$ depth predictions illustrate the redundancy provided by multiple sensor responses, enabling the robustness of the skin to single damages. As stated in this previous work,^[35] it is obvious that this redundancy is limited and losses of multiple fibers will decrease sensitivity rapidly, indicating the importance of striving for correct healing on the material level in electronic skins that are damaged for multiple times in application. Although recalibration through full retraining is very successful, it poses challenges in future applications due to extensive sampling. The following section looks at how a pretrained network's prior knowledge can be utilized to quickly produce similarly performing models when additional recalibration data is costly i.e., avoiding the need for 5000 new data samples after damage/healing.

2.8. Transfer Learning for Healed Skin Recalibration

In the previous section, we saw how changes in sensor properties introduced by the healing process cause significant degradation in the performances of networks trained on the undamaged skin. Networks trained on 4500 new physical sensor responses measured from the healed skin show no such degradation, demonstrating excellent localization and depth prediction capabilities. These secondary networks are trained ‘from scratch’, with no prior knowledge, and thus they require the same amount of data to reach these levels of performance. As discussed in the introductory sections, such full recalibration of a bioinspired soft sensor is likely to be costly in time, resources, and energy. Instead, it is often beneficial to quickly produce a reasonably performing model with minimal recalibration data, avoiding the ‘downtime’ in which no functioning model is available. To investigate this, we continue the training of the undamaged skin's network, which adapts to the healed sensor nonlinearities. In order to encourage the quick convergence of the network on a satisfactory solution, we analyze the performance of transfer learning techniques on two aspects (discussed fully in Materials and Methods):

1. **Layer freezing.** The learn rates of up to three of the hidden layers are set to zero before training continues, reducing the total number of weights & biases for optimization.
2. **Tactical selection.** Four methods of selecting the x - y coordinates of new samples are compared: arranged in a uniform grid over the surface of the skin; fully random; weighted in 1D such that y coordinates close to the damaged sensor are more likely to be selected; and weighted in 2D, such that points closest to the damaged location are more likely to be selected.

Figure 5 presents the utility of these techniques in adapting to the healed skin based on the average error and the percentage of correct depths, after the two most severe damage cases: cases 2 & 3, represented in **Figure 5** and **Figure 6**, respectively. Grey dotted lines indicate the performance of a network trained with no prior knowledge. Learning with each parameter set is repeated three times; the ranges of the average localization error and depth predictions are marked, with plotted lines following the mean values.

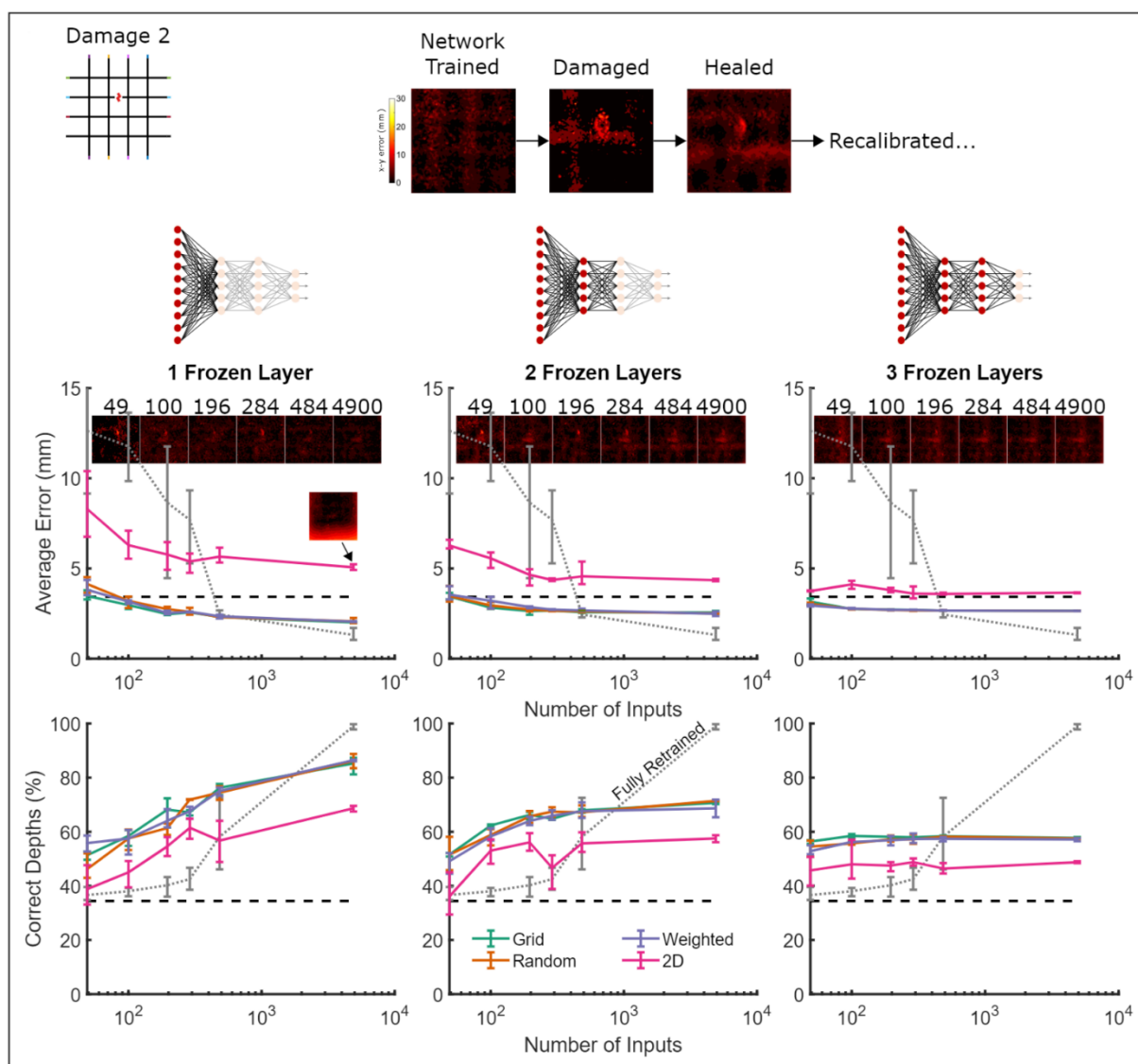


Figure 5: Performance of the networks' transfer learning for damage 2. After ‘freezing’ the weights of selected fully connected layers, training of the networks is continued using 49, 100, 196, 284, 484, or 4900 new data points. Four methods of selecting these points - grid, random, weighted, and 2D (see methods) - are compared to the ‘fully retrained’ performance which has no prior knowledge. A dashed horizontal line represents the performance of the pretrained networks before transfer learning begins (i.e., number of sample points = 0). Example mappings of x - y localization error are shown for the random selection method.

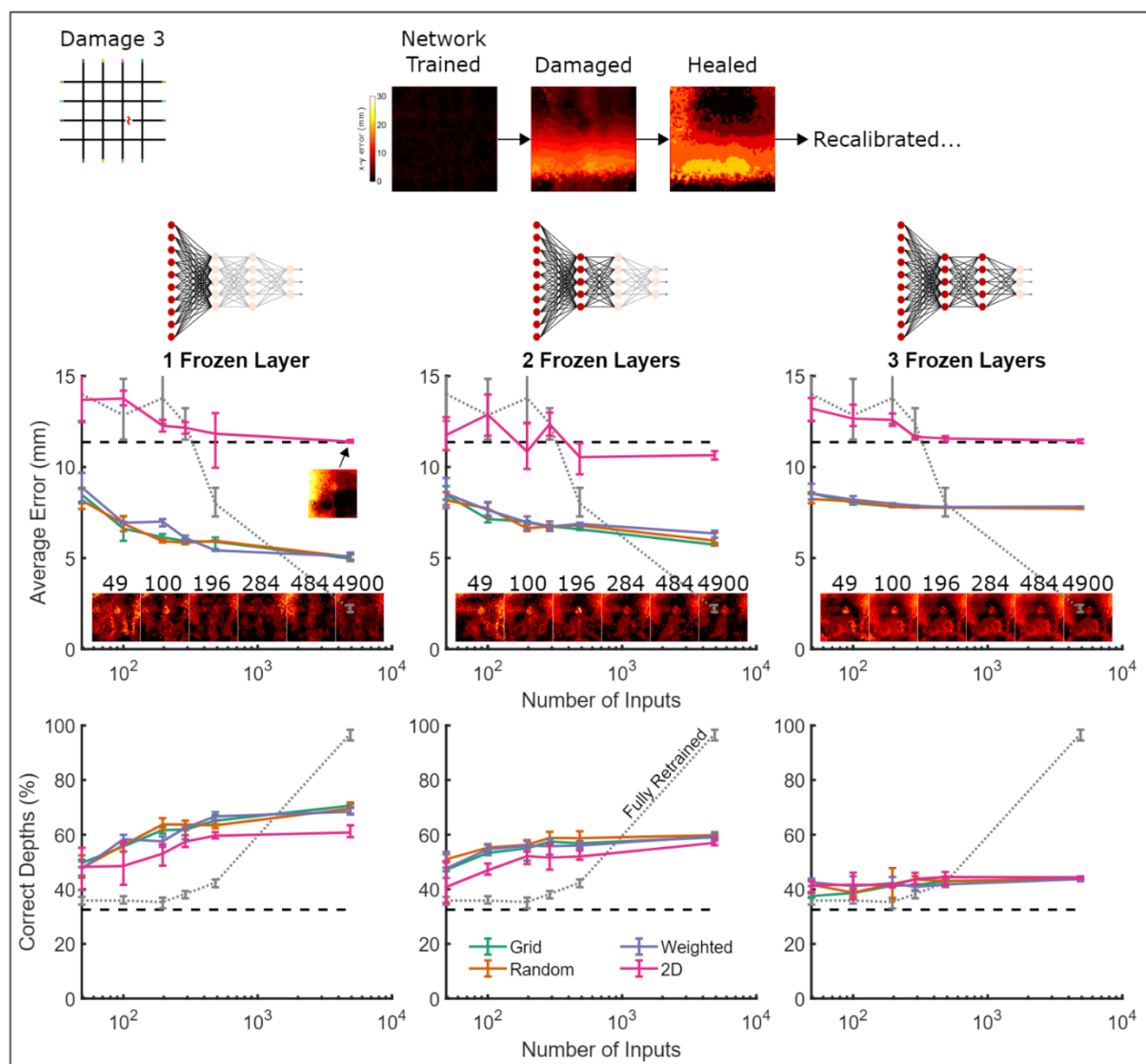


Figure 6: Performance of the networks' transfer learning for damage 3. After 'freezing' the weights of selected fully connected layers, training of the networks is continued using 49, 100, 196, 284, 484, or 4900 new data points. Four methods of selecting these points - grid, random, weighted, and 2D (see methods) - are compared to the 'fully retrained' performance which has no prior knowledge. A dashed horizontal line represents the performance of the pretrained networks before transfer learning begins (number of sample points = 0). Example mappings of x - y localization error are shown for the random selection method.

Figure 5 looks at the adaptation of a pre-trained network to the second healed case, having been trained on 4500 data points before damage. Without any form of retraining, we have seen from **Figure 4A** that an average x - y error of 3.21 mm & depth-prediction accuracy of 34.3% are achieved, marked with a horizontal dashed line in the 6 plots. After being provided with just 49 new sample points, the networks' localization performances generally remain very close to this line, with one exception: the 2D Gaussian method of selection (represented in pink) performs consistently poorly throughout the tests. To explain why, the first plot includes an

image of the localization errors when 4900 samples are used for the transfer learning. Since the region directly surrounding the damage has been favored during sample selection, a consistently low error is now found here, as designed. However, this comes at the cost of higher error in the lesser sampled areas - in this case, the left, right, and bottom edges of the sensorized skin. This Gaussian method is therefore a good choice when we wish to design a sensor network with areas of higher and lower sensitivity, and could be extended to include more complex 2D functions. Since our model focuses on global optimization of sensitivity, the 2D method is not the best option - additional experiments could consider the effect of standard deviation on its performance.

Using one of the remaining transfer learning methods appears to be a much better choice than full retraining when smaller numbers of sampling are favored: all the methods outperform the network with no prior knowledge below approximately 400 sample points; if only depth prediction is necessary, this figure is closer to 1000. As expected, all performances tend to improve as the number of samples increases, and the benefits of full retraining over a quicker transfer method only become significant when thousands of sample points are available.

There is surprisingly little difference between the performances of the grid, random, and weighted methods - especially at higher sample points. It should be noted that the 1D weighted implementation is less severe than that of the under-performing 2D Gaussian method. The fact that only the 2D method is clearly separate from the others suggests that global, rather than local, calibration is necessary for successful short-term transfer. Provided the network continues learning from a sufficiently uniform distribution over the skin plane, the method of selection (grid, random, or weighted) does not appear to make a significant difference.

Figure 5's three columns consider the magnitude of layer freezing upon performance, setting the learn rates of one, two, or three of the hidden layers to zero before transfer learning commences. In the extremely short term (49/100 sample points), freezing all 3 layers - leaving only the output layer to be adapted - produces the best-performing network. Indeed, the 49-sample grid, random, and weighted methods of the first two columns show slight decreases in localization performance compared to the zero-sample case, whilst three frozen layers consistently improve localization. However, the limited change in input→output mapping that can be changed using only the third layer weights leads to a quick saturation of this column's performance, whilst the single frozen layer continues to improve for larger samples. Unsurprisingly, 2 frozen layers produces a set of results lying between these two extremes, forming a reasonable compromise when the number of available sample points is unknown.

Figure 6 shows a similar set of patterns in adapting to the more severe damage/healed case. Again, the 2D method does not satisfactorily converge, overfitting to the damaged area at the expense of sensitivity in more remote regions. The remaining 3 more uniformly distributed transfer methods are near-indistinguishable, outperforming the fully retrained network for fewer than ~ 1000 samples. However, 49 samples are now sufficient for all three methods to significantly improve upon the zero-sample case; the localization maps show that the region of significant error above the damaged sensor quickly vanishes, and could simply be the result of small shifts in baseline resistance. As such, freezing all three layers is no longer the best approach for small sample sizes, and the 1 frozen layer network produces the best performance in every case. Its greatest improvement upon the fully retrained network occurs with 196 samples, where the random transfer learning technique improves the average localization accuracy by 7.9 mm, and the accuracy of depth predictions by 28.4 %.

3. Discussion

Although many studies have proven the potential of healable soft sensors, all these works are limited to the recovery of electrical properties after damage and have not investigated the functional integrity of the sensors after a damage-heal cycle. This is mainly because of the challenges involved in modelling these highly non-linear and time-variant polymer composites. The proposed learning-based framework circumvents this challenge using real-world experience. The use of deep neural networks with sensor responses resulted in a high-resolution electronic skin able to localize touch with a high resolution of 2 mm and a correct depth estimation of nearly 100%, even with these highly non-linear healable sensor fibers. This clearly illustrates the capacity of machine-learning, which use will be inevitable in the calibration of many future healable soft sensors.

In order to truly enhance longevity of healable sensors and the systems in which they are embedded, healing of damages should involve minimal sensitivity deterioration. Although full restoration of the sensor response at room temperature is possible upon excellent recontact, its recovery is highly influenced by the slightest misalignment or insufficient contact. In future applications that demand autonomous healing and multiple damage-healing cycles, these non-optimal recontacts will be unavoidable. In these cases, healing by heating can fill the resulting microscopic cavities, increasing the contact and the healing efficiency. However, this thermal treatment impacts the base resistance and the sensor response of the healed fiber and the

undamaged fibers. Consequently, the sensitivity decreases and in particular the depth estimation becomes unreliable. In these cases, recalibration is inevitable to preserve sensor sensitivity.

In this paper, it is shown that full resampling and retraining of the network on the healed electronic skin regains original performance, and even improves it in some cases. In addition, the proposed approach also allows us to exploit redundancies in the system upon loss of a sensor fiber, which provides an additional temporary robustness to damages. This is however limited, as the loss of multiple fibers will eventually drive down accuracy, highlighting the need for physical healing abilities, in particular for applications where damage is recurrent. Consequently, the authors believe that the combination of machine learning and self-healing can provide robust and long-lived soft sensorized systems able to cope with multiple types of damage via healing on the material level and adaptation on the software level.

Although training from scratch is reliable, it limits future applications as it will be time-consuming and costly. Though not explored in this work, the authors expect the 'press-and-release' method of sampling to be relatively robust to changes in press duration, enabling quicker sampling procedures to be designed. Ultimately, this will be limited by the recovery period of the material. Secondly, to eliminate unnecessary recalibration, health monitoring is extremely important. As presented in the paper, damage can be detected by monitoring the loss of electrical contact of the fiber resistances, while damage localization in the millimeter scale can be performed by probing along the damaged fiber. This can also detect if the damage is healed autonomously at room temperature. For these damages, heating is not required as it would not further increase recovery, on the contrary it decreases sensitivity and results in the need for recalibration. In addition, in actual future applications, including soft robots and smart wearables, tracking the locations of damage provides important information about parts and locations that are prone to damage.

The introduced transfer learning approach presents a fast alternative for model adaptation with reduced data points. Freezing a higher number of layers in the network is desirable when working with fewer data points and vice versa. The advantages of the proposed transfer learning approach will become more relevant as the sensor network becomes increasingly larger. In such cases, the amount of data required for full training would be much higher. Additionally, damages and healing would be more localized, implying that a larger chunk of the prior model can be recycled. In that scenario, the resampling algorithm can also become relevant, which is not found in our experiments. Targeting the sampling near to the damage area, or around the

damaged sensor, did not lead to improved transfer learning compared to random sampling. This is due to the change in baseline resistance of all fibers due to heating, leading to changes in sensory response throughout the entire skin. Consequently, the resampling and retraining strategy will highly depend on the application in which the sensor skin is used and the time at which damages occur. Transfer learning with a high number of frozen layers can be used to restart operation quickly after healing, with a slightly reduced performance. On the other hand, full retraining can be performed during inactive periods of the system as it requires more time, eventually recovering full sensitivity of the electronic skin.

Although polymeric soft sensors and electronic skins can be produced very cheaply, the authors believe that recovery of the skin after damage through material based healing whether or not in combination with compensation through recalibration, can provide an economic alternative to replacement in various future applications. This is the case when electronic skins are integrated in complex systems. Although the components can be cheap, replacement or maintenance can still be very expensive, due to extensive (dis)assembly. These disassembly issues are exacerbated by the fact that creating modular, scalable soft robots and systems is very challenging, and components are generally irreversibly bond or cured together. In addition, whereas recovery through healing and adaptation can be done autonomously by the system, replacement will in most cases be done through external intervention. For remote applications and field (soft) robotics, external interventions can be very costly as they would rely on transporting the replacement parts to the system or the system to a repair station. Consequently, the authors believe that the presented combination of material-based healing and software-based adaptation/compensation, can be an enabling technology for many soft robotics and soft devices, of which their adoption is currently prevented by their lack of resilience to damage.

4. Experimental Section/Methods

Materials: The self-healing material, used to insulate the conductive fibers in the sensor matrix is composed of a Diels-Alder network polymer. The network is formed by crosslinking between bismaleimide (BMI1400 or DPBM) and furan-compounds (FT3000 or FT5000). BMI1400 is a low viscosity bismaleimide oligomer with an average molecular weight of 1715 g.mol^{-1} and a maleimide functionality of two and supplied by Caplinq. DPBM is 1,1'-(methylenedi-4, 1-phenylene) bismaleimide with a purity of 95% is obtained from Sigma Aldrich. FT3000 and FT5000 are furan-functionalized Jeffamines, obtained through an epoxy amine reaction between furfuryl glycidyl ether (FGE) and Jeffamine JT3000 or JT5000. JT3000 and JT5000 are

polyetheramine obtained from Huntsmann from the Jeffamine T-series triamines, with a molecular weight of respectively 3180 g.mol⁻¹ and 5712 g.mol⁻¹. FGE has a purity of 97% and is supplied by Sage Chemicals. By mixing two reactive compounds, furan-functionalize Jeffamine JT3000 or JT5000 (**Figure 1A, B**: blue) and bismaleimide DPBM or BMI1400 (red), the Diels-Alder reaction forms thermoreversible covalent crosslinks and an elastomeric polymer network (**Figure 1B**). The non-conductive BMI1400-FT3000-r0.5, used as insulating matrix in the sensors, is obtained via polymerization of a mixture of BMI1400 and FT3000 with a maleimide-to-furan stoichiometric ratio r of 0.5. The conductive DPBM-FT5000-r0.6-20wt%CB260, used to manufacture the fibres, is synthesized via solvent casting a mixture of DPBM and FT5000 with a maleimide-to-furan stoichiometric ratio r of 0.6 and 20wt% carbon black CB260, dissolved in chloroform with a 20wt%. The synthesis of both of these polymer networks described in detail in **Supporting information 1**.

Healable Artificial Skin: The sensor network (**Figure 1D**) is a 55x55x5 mm³ square composed out of BMI1400-FT3000-r0.5 in which eight conductive DPBM-FT5000-r0.6-20wt%CB260 fibers are integrated in a grid-based morphology. Four fibers are embedded straight in the x-directions with a distance of 11 mm between them and at a depth of 2.5 mm. The other fibers are embedded perpendicular to these, in the y-direction, also with a distance of 11 mm between them, but at a depth of 3.5 mm. Consequently, perpendicular fibers do not touch in the matrix. The fibers have a diameter of 0.5 mm and are extruded in a dedicated piston extruder (**Supporting information 2**). The sensor network is manufactured by straightening the fibers in a laser cut PMMA mold, in which a mixture of BMI1400 and FT3000 is poured (**Supporting information 3**). Upon polymerization of this BMI1400-FT3000-r0.5 mixture, the matrix solidifies and the fibers are embedded. During this polymerization, strong covalent Diels-Alder bonds are formed between the fibers and the matrix. At the ends of the sensor network, the fibers are connected to jump wires via aluminum crimp connectors.

Characterization: The two Diels-Alder polymer networks are characterized via tensile testing until fracture with a strain ramp of 1% s⁻¹ on a Dynamic Mechanic Analyzer (DMA) Q800 of TA instruments and sample sizes of 5x30x1 mm³ for the BMI1400-FT3000-r0.5 samples and 3x30x1 mm³ for the DPBM-FT5000-r0.6-20wt%CB260. The single resistive strain sensor is characterized on a dedicated tensile testing setup. The sensor network is characterized via training data collected using a UR5 arm from Universal Robots equipped with a cylindrical polylactic acid (PLA) probe end effector with a diameter of 5 mm (**Figure 1A**). The skin is

adhered to a 3 mm PMMA plate, which is secured to the table below the probe. The 3D origin is set above the intersection of sensors 4 & 8 in **Figure 2**, such that sensor 4 lies in the $x=0$ plane and sensor 8 lies in the $y=0$ plane. The $z=0$ plane is defined at the skin's free surface. All descents and ascents begin from the $z=10$ mm plane, in which the probe moves between x - y coordinates.

A full characterization of the skin (undertaken after every damage/healing) consists of three parts:

1. *Line:* (25 minutes) 100 equally-spaced points along the most recently damaged sensor are consecutively probed at a 1.5 mm depth, and all sensor responses are recorded. During each, the probe descends vertically downwards at 3.8 mm.s^{-1} , is held in place for 5 seconds, before vertically ascending at 7.7 mm.s^{-1} . The setup pauses for 6 seconds between each probe to minimize the transient effects of the skin's recovery. The 80 inputs to the neural network can be collected at the start of this wait period, and do not depend on its length. The response recoveries are generally observed to take approximately 1s, and it is expected that this wait could be significantly shortened in future experiments. Animations of the sensor responses can be found in Movies S3 and S4.
2. *Repeated:* (16 minutes) The closest intersection of 2 points to the damaged location is probed 100 times at a 1mm depth, and all sensor responses are recorded. The probe descends and ascends at 7.3 mm.s^{-1} , pressing for 5 s and leaving 2s between each press. Animations of the sensor responses can be found in Movies S5 and S6.
3. *Random:* (17 hours) 5000 random x - y coordinates are generated within the red square of **Figure 2A**, with each randomly allocated to a depth of 0.5, 1.0, or 1.5 mm. All locations are probed, using the same timings described above (plus additional movement between locations), and all 8 sensor responses are recorded. These 5000 responses are used to train the neural networks (90:10% training:validation split), to plot the error maps, and to calculate the network's performance.

Each of the eight sensors is connected to the ground side of a potential divider, with 120 k Ω resistors completing the connection to a 5 V direct current (DC) output of a National Instruments multi-channel data acquisition module-USB-6212. Throughout the characterization, sensor responses are recorded at the central nodes of the potential dividers, using the USB-6212's analog inputs at a 20 Hz sampling rate. As such, the mapping between a sensor's plotted voltage V and the measured resistance R is described

$$R = 120 \cdot \frac{V}{5 - V} k\Omega$$

The 80 inputs of the neural network are sampled from the 8 sensors' raw voltage measurements at 10 specific times after the probe begins to descend: 1.25, 1.50, 1.75, 2.00, 2.25, 6.50, 6.75, 7.00, 7.25, & 7.50 s. The 24-input case in **Figure 2D** instead samples the 8 sensor voltages at 1, 3, & 8 s, after using total variation denoising ($\lambda = 15$) to convert the response to a square wave.^[35,48] Intermediate numbers of inputs are considered in Figure S2: network performances are found to have saturated before the 80-input case, such that higher input numbers are not investigated in this work. Damaging events, e.g. cuts in the sensor network, are recorded using a digital camera.

Healing: Upon excellent contact and limited misalignment of the fracture surfaces, healing can be performed at room temperature.^[44] However, the rebonding and the resulting healing is accelerated by increasing the temperature, which increases both reactivity and kinetics in the dynamic polymer network.^[49] For healing on the material level, on the single sensor level and on the artificial skin level, always the same temperature profile was used; 1 hour at 90°C. Upon cooling to 25°C and remaining for 24 hours, the Diels-Alder bonds rebond, eventually recovering mechanical performance. Heat was provided by placing the damaged parts in a preheated oven at 90°C.

Deep Neural Network: The same network architecture is used throughout the work, implemented using *MATLAB*'s Deep Learning Toolbox, and is shown in **Figure 2C**. The preliminary input layer is of size 80 in all cases other than the creation of **Figure 2D**'s 24-input map. Between this and the 3-node regression output (x, y, & depth), three fully connected layers (of sizes 20, 10, 10) are implemented, using tanh, tanh, & ReLU activation functions, respectively.

To train the network on 5000 measured probes, the input dataset is first normalized using the mean and standard deviations of each of the 80 inputs. The corresponding targets are linearly scaled to range between 0 & 1, such that depth and positional accuracies are assigned equal importance. An adaptive moment estimation optimizer is used with 90:10% training:validation split, 0.05 learn rate, and gradient threshold of 1. Training is terminated when the validation loss (calculated every 30 iterations) does not improve over 10 consecutive evaluations. If training exceeds 1250 iterations, the learn rate is dropped to 0.01; training is terminated if 2000

iterations pass. In practice, the only network which does not fulfill the validation criterion before the learn rate drops is that of **Figure 4C**, as seen in Figure S4.

Transfer learning is performed by 'freezing' a specified number (1, 2, or 3) of the pretrained network's fully connected hidden layers i.e. setting their learn rates to zero. Training is continued using the parameters described above, with an increased gradient threshold of 10. Four methods are introduced to select a subset of the available data for training & validation, representing the strategic choice of recalibration points after sensor damage & healing:

1. *Grid*: The x - y coordinates of the selected recalibration points form a geometric grid, with edges corresponding to those of **Figure 2A**'s red zone; only square numbers are tested in **Figure 5** and **Figure 6**, in order to facilitate this.
2. *Random*: The points are sampled randomly from the available dataset.
3. *Weighted*: The x coordinate is sampled randomly, whilst the y coordinate is sampled from a truncated Gaussian distribution centred on the damaged sensor, with 15mm standard deviation.
4. *2D*: The coordinates are sampled from a truncated 2D Gaussian, centred at the damaged location with $\sigma = 20.I_2$.

Once a list of coordinates has been generated for the grid, weighted, and 2D cases, the closest pre-probed point is identified, and used as an input for transfer learning. Probing depths remain randomly distributed between 0.5, 1.0, & 1.5 mm.

Supporting Information

Supporting Text 1: Synthesis of the self-healing polymer and composite.

Supporting Text 2: Fiber manufacturing via piston extrusion.

Supporting Text 3: Manufacturing of the electronic skin via casting.

Figure S1: Performances of ten networks with different input size, trained, validated, and tested on the undamaged sensor.

Figure S2: Performance of a 70-input network trained, validated, and tested on the skin after the first damage case.

Figure S3: Initial training progress to the 5000 undamaged sensor responses (90:10% training:validation split), for networks with 24-neuron and 80-neuron input layers/

Figure S4: Training progresses of the 'no prior knowledge' (from scratch) networks to the three healed skin states.

Movie S1: A quickened video of the random probing process.

Movie S2: Synchronizations of the voltage responses from each sensor's potential divider (0 → 5 V) during the three damage cases.

Movie S3: Responses of the three damaged skin states to probes along the lengths of the damaged sensor.

Movie S4: Responses of the three healed skin states to probes along the lengths of the damaged sensor.

Movie S5: Responses of the three damaged skin states to repeated probes at a sensory junction near the damaged area.

Movie S6: Responses of the three healed skin states to repeated probes at a sensory junction near the healed area.

Acknowledgements

Funding: This work was performed in relation to and funded by the EU FET Open RIA Project SHERO (828818). In addition, the authors gratefully acknowledge the FWO (Fonds Wetenschappelijk Onderzoek) for the personal grants of Terryn (1100416N) and Roels (1S84120N), and EPSRC DTP EP/R513180/1.

Author contributions: S.T., D.H., T.G.T., F.I., conceived the conceptual idea of combining self-healing with machine learning to develop electronic skins that preserve their sensitivity after damages, combining material-level healing with software-level adaptation. S.T., D.H., T.G.T. designed the methodology and experiments. S.T. fabricated the electronic skin. S.T., E.R., F.S. manufactured the fibres. S.T., D.H., T.G.T. did experiments and did data treatment and interpretation. S.T., D.H. did the visualization through videos, pictures and figures for manuscript and Supporting Information. S.T., D.H., T.G.T. wrote the original draft of the manuscript. All authors contributed in review & editing. F.I. did supervision. S.T., F.I. did funding acquisition.

Competing interests: Authors declare that they have no competing interests.

Data and materials availability: All data are available in the main text or the supporting information.

References

- [1] N. Lu, D. H. Kim, *Soft Robot.* **2014**, *1*, 53.
- [2] M. Amjadi, K. U. Kyung, I. Park, M. Sitti, *Adv. Funct. Mater.* **2016**, *26*, 1678.
- [3] H. Wang, M. Totaro, L. Beccai, *Adv. Sci.* **2018**, *5*.
- [4] S. Li, X. Zhou, Y. Dong, J. Li, *Macromol. Rapid Commun.* **2020**, 2000444.
- [5] Y. Park, B. Chen, R. J. Wood, **2012**, *12*.
- [6] M. Amjadi, A. Pichitpajongkit, S. Lee, S. Ryu, I. Park, *ACS Nano* **2014**, *8*, 5154.
- [7] Z. Zhu, H. S. Park, M. C. McAlpine, *Sci. Adv.* **2020**, *6*, 1.
- [8] H. Zhao, J. Jalving, R. Huang, R. Knepper, A. Ruina, R. Shepherd, *IEEE Robot. Autom. Mag.* **2016**, *23*, 55.
- [9] M. Khatib, O. Zohar, H. Haick, *Adv. Mater.* **2021**, *33*, 1.
- [10] J. Kang, J. B. H. Tok, Z. Bao, *Nat. Electron.* **2019**, *2*, 144.
- [11] M. U. Ocheje, B. P. Charron, A. Nyayachavadi, S. Rondeau-Gagné, *Flex. Print. Electron.* **2017**, *2*, 043002.
- [12] Y. J. Tan, J. Wu, H. Li, B. C. K. Tee, *ACS Appl. Mater. Interfaces* **2018**, *10*, 15331.
- [13] S. Terryn, J. Langenbach, E. Roels, J. Brancart, C. Bakkali-Hassani, Q.-A. Poutrel, A. Georgopoulou, T. G. Thuruthel, A. Safaei, P. Ferrentino, *Mater. Today* **2021**, *47*, 187.
- [14] S. Terryn, J. Brancart, D. Lefeber, G. Van Assche, B. Vanderborght, *IEEE Robot. Autom. Lett.* **2017**, *3*, 16.
- [15] P. Zhang, G. Li, *Polymer (Guildf)*. **2015**, *64*, 29.
- [16] Z. Feng, J. Hu, H. Zuo, N. Ning, L. Zhang, B. Yu, M. Tian, *ACS Appl. Mater. Interfaces* **2019**, *11*, 1469.
- [17] E. Palleau, S. Reece, S. C. Desai, M. E. Smith, M. D. Dickey, *Adv. Mater.* **2013**, *25*, 1589.
- [18] Y. L. Rao, A. Chortos, R. Pfattner, F. Lissel, Y. C. Chiu, V. Feig, J. Xu, T. Kurosawa, X. Gu, C. Wang, M. He, J. W. Chung, Z. Bao, *J. Am. Chem. Soc.* **2016**, *138*, 6020.
- [19] J. Y. Oh, S. Rondeau-Gagné, Y. C. Chiu, A. Chortos, F. Lissel, G. J. N. Wang, B. C. Schroeder, T. Kurosawa, J. Lopez, T. Katsumata, J. Xu, C. Zhu, X. Gu, W. G. Bae, Y. Kim, L. Jin, J. W. Chung, J. B. H. Tok, Z. Bao, *Nature* **2016**, *539*, 411.
- [20] J. Kang, D. Son, G. J. N. Wang, Y. Liu, J. Lopez, Y. Kim, J. Y. Oh, T. Katsumata, J. Mun, Y. Lee, L. Jin, J. B. H. Tok, Z. Bao, *Adv. Mater.* **2018**, *30*, 1.
- [21] B. C. Tee, C. Wang, R. Allen, Z. Bao, *Nat. Nanotechnol.* **2012**, *7*, 825.
- [22] D. Son, J. Kang, O. Vardoulis, Y. Kim, N. Matsuhisa, J. Y. Oh, J. W. To, J. Mun, T. Katsumata, Y. Liu, A. F. McGuire, M. Krasen, F. Molina-Lopez, J. Ham, U. Kraft, Y.

- Lee, Y. Yun, J. B. H. Tok, Z. Bao, *Nat. Nanotechnol.* **2018**, *13*, 1057.
- [23] Y. Cao, Y. J. Tan, S. Li, W. W. Lee, H. Guo, Y. Cai, C. Wang, B. C. K. Tee, *Nat. Electron.* **2019**, *2*, 75.
- [24] E. D'Elia, S. Barg, N. Ni, V. G. Rocha, E. Saiz, *Adv. Mater.* **2015**, *27*, 4788.
- [25] Y. Yang, B. Zhu, D. Yin, J. Wei, Z. Wang, R. Xiong, J. Shi, Z. Liu, Q. Lei, *Nano Energy* **2015**, *17*, 1.
- [26] D. Hardman, T. George Thuruthel, F. Iida, *NPG Asia Mater.* **2022**, *14*.
- [27] J. Li, J. Liang, L. Li, F. Ren, W. Hu, J. Li, S. Qi, Q. Pei, *ACS Nano* **2014**, *8*, 12874.
- [28] Y. He, S. Liao, H. Jia, Y. Cao, Z. Wang, Y. Wang, *Adv. Mater.* **2015**, *27*, 4622.
- [29] S. Bai, C. Sun, H. Yan, X. Sun, H. Zhang, L. Luo, X. Lei, P. Wan, X. Chen, *Small* **2015**, *11*, 5807.
- [30] T. G. Thuruthel, A. W. Bosman, J. Hughes, F. Iida, *MDPI Sensors* **2021**, *21*, 8284.
- [31] D. Kim, S. H. Kim, T. Kim, B. B. Kang, M. Lee, W. Park, S. Ku, D. W. Kim, J. Kwon, H. Lee, J. Bae, Y. L. Park, K. J. Cho, S. Jo, *PLoS One* **2021**, *16*, 1.
- [32] B. Shih, D. Shah, J. Li, T. G. Thuruthel, Y. L. Park, F. Iida, Z. Bao, R. Kramer-Bottiglio, M. T. Tolley, *Sci. Robot.* **2020**, *5*.
- [33] S. Han, T. Kim, D. Kim, Y. L. Park, S. Jo, *IEEE Robot. Autom. Lett.* **2018**, *3*, 873.
- [34] T. G. Thuruthel, B. Shih, C. Laschi, M. T. Tolley, *Sci. Robot.* **2019**, *4*, eaav1488.
- [35] T. G. Thuruthel, J. Hughes, F. Iida, *IEEE Sens. J.* **2020**, *1*.
- [36] T. G. Thuruthel, J. Hughes, A. Georgopoulou, F. Clemens, F. Iida, *IEEE Robot. Autom. Lett.* **2021**, *6*, 2099.
- [37] D. Kong, G. Yang, G. Pang, Z. Ye, H. Lv, Z. Yu, F. Wang, X. V. Wang, K. Xu, H. Yang, **2022**, 2200050.
- [38] Z. Husain, N. A. Madjid, P. Liatsis, *IEEE Sens. J.* **2021**, *21*, 11628.
- [39] K. S. Sohn, J. Chung, M. Y. Cho, S. Timilsina, W. B. Park, M. Pyo, N. Shin, K. Sohn, J. S. Kim, *Sci. Rep.* **2017**, *7*, 1.
- [40] J. W. Lee, J. Chung, M. Y. Cho, S. Timilsina, K. Sohn, J. S. Kim, K. S. Sohn, *ACS Appl. Mater. Interfaces* **2018**, *10*, 20862.
- [41] M. Y. Cho, J. H. Lee, S. H. Kim, J. S. Kim, S. Timilsina, *ACS Appl. Mater. Interfaces* **2019**, *11*, 11910.
- [42] S. Wang, M. W. Urban, *Nat. Rev. Mater.* **2020**, *5*, 562.
- [43] A. Cuvelier, R. Verhelle, J. Brancart, B. Vanderborght, G. Van Assche, H. Rahier, *Polym. Chem.* **2019**, *10*, 473.
- [44] S. Terryn, J. Brancart, E. Roels, G. Van Assche, B. Vanderborght, *IEEE Robot. Autom.*

Mag. **2020**, 27, 44.

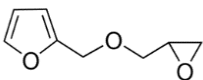
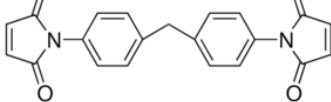
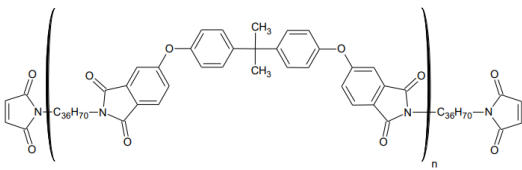
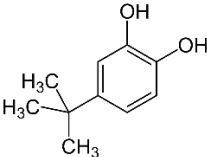
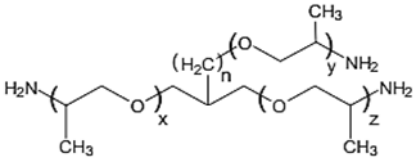
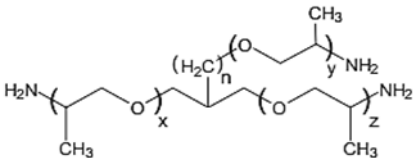
- [45] N. Tiwari, Ankit, M. Rajput, M. R. Kulkarni, R. A. John, N. Mathews, *Nanoscale* **2017**, 9, 14990.
- [46] L. Flandin, A. Hiltner, E. Baer, *Polymer (Guildf)*. **2001**, 42, 827.
- [47] S. J. Pan, Q. Yang, *IEEE Trans. Knowl. Data Eng.* **2010**, 22, 1345.
- [48] M. A. Little, N. S. Jones, *Proc. R. Soc. A Math. Phys. Eng. Sci.* **2011**, 467, 3088.
- [49] S. Terryn, J. Brancart, D. Lefeber, G. Van Assche, B. Vanderborght, *Sci. Robot.* **2017**, 2.

Supporting Information

Supporting Information 1: Synthesis of the self-healing polymer and composite.

Seppe Terryn

Chemical composition of the reagents.

Abbreviation	Name & Structure	Supplier & Properties
Dienophile: Furan		
FGE	furfuryl glycidyl ether 	Sigma-Aldrich (96 %) Sagechem (96%) $M = 154.16 \text{ g mol}^{-1}$ $f_{\text{epoxy}} = 1$ $M^* = 154.16 \text{ g eq}_{\text{epoxy}}^{-1}$ $\rho = 1.122 \text{ g ml}^{-1}$
Deine: Maleimide		
DPBM	1,1'-(methylenedi-4,1-phenylene)bismaleimide 	Sigma-Aldrich (95 %) $M = 358.36 \text{ g mol}^{-1}$ $f_M = 2$ $M^* = 188.61 \text{ g eq}_M^{-1}$ $T_m = 151 \text{ }^\circ\text{C}$
BMI1400		Designer Molecules $M = 1719 \text{ g mol}^{-1}$ $f_M = 2$ $M^* = 859.5 \text{ g eq}_M^{-1}$
Radical Inhibitor		
TBC	4-tert-butylcatechol 	Sigma-Aldrich (99%) $M = 166.22 \text{ g mol}^{-1}$ $T_m = 55 \text{ }^\circ\text{C}$
Triamine Jeffamines		
JT3000		Aurora Chem (100 %) $x + y + z = 54.2$ $M = 3180 \text{ g mol}^{-1}$ $f_{\text{NH}} = 6$ $M^* = 530 \text{ g eq}_{\text{NH}}^{-1}$ $n=0$
JT5000		Huntsmann (100 %) $x + y + z = 96.8$ $M = 5712 \text{ g mol}^{-1}$ $f_{\text{NH}} = 6$ $M^* = 952 \text{ g eq}_{\text{NH}}^{-1}$ $n=0$

Synthesis:

The synthesis of the Diels-Alder polymer and composite consists of two synthesis steps. The first step is identical for the polymer and the composite, while the second step is carried out differently, as a different maleimide is used.

Step 1: The furfuryl glycidyl ether (FGE) is irreversibly bonded to the Jeffamine (Jx) by way of an epoxy-amine reaction, yielding a furan-functionalized Jeffamine (FT3000 or FT5000)

Step 2: The furan groups on the furan-functionalized Jeffamine are reacted with the maleimide groups on a bismaleimide to form DA-crosslinks that form a thermoreversible network.

In what follows, these two steps are described in more detail. In the first step, furfuryl glycidyl ether is reacted with a selected Jeffamine through an irreversible epoxy-amine reaction. This reaction is performed under stoichiometric conditions ($r = n_{NH} / n_{epoxy} = 1$). The more viscous Jeffamine and the low viscosity FGE are poured in an amber colored glass vial. The contents are mixed using a magnetic stirrer. As these two compounds mix well, there is no need for a solvent. The mixed vial is placed in an oven for 7 days at 60 °C, a temperature at which the epoxy-amine reaction takes place without the need of a catalyst. During these 7 days, to ensure mixing, every 24 hours the vial is placed on a magnetic stirrer for 30 min, after which it is replaced in the oven. Next, to complete the reaction, the mixture is kept at 90 °C for 2 days.

In the second step, the FFJ was reacted with a bismaleimide to form the DA crosslinks of the reversible covalent network. Depending on the preferred material properties this synthesis step can be performed in stoichiometric ($r = n_M / n_F = 1$) or excess furan ($r < 1$) conditions. This step is different for the polymer and the composite:

Diels-Alder polymer: BMI1400-FT3000-r0.5: BMI1400 is placed together with radical inhibitor 4-tert-butylcatechol (5wt% of BMI1400) in a glass container. In order to melt the 4-tert-butylcatechol crystals and to improve mixing by reducing the viscosity of BMI1400, the mixture is heated to 80 °C. Next the BMI1400+inhibitor is mixed with FT3000 according to a

stoichiometric ratio ($r = n_M / n_F = 0.5$) by a spatula. Next the mixture is degassed using a vacuum. The mixture is poured in a mold and left to cure/polymerize for 24 hours.

Diels-Alder composite: DPBM-FT5000-r0.6-20wt%CB260: The bismaleimide (DPBM) is crystalline ($T_m = 151\text{ }^{\circ}\text{C}$). These crystals do not dissolve in the furan-functionalized Jeffamine (even with heating to $120\text{ }^{\circ}\text{C}$). To facilitate the mixing of the reagents, chloroform (CHCl_3) was used as a solvent. This synthesis step starts by dissolving FFJ and bismaleimide, in (non-)stoichiometric quantities, in chloroform with a weight percentage of 20 wt% of solute. 4-Tert-butylcatechol (5 wt% compared to DPBM) is added to this mixture. This 4-tert-butylcatechol acts as a radical inhibitor for the homopolymerization of maleimide at higher temperatures. The CB260 is added as well with a 20wt%. All components are added to a well-sealed container that is placed on a mechanical stirrer for 24 hours to ensure that all bismaleimide is dissolved and all CB260 particles are well dispersed. The chloroform is extracted from this mixture in a vacuum oven that is equipped with a liquid nitrogen cold trap to prevent solvent entering the rotary vacuum pump. This vacuum oven is first preheated to $60\text{ }^{\circ}\text{C}$. The mixture is poured into a Teflon mold and placed in the preheated oven. To start the extraction of CHCl_3 , the pressure is first lowered down to 600 mbar. One should not increase the temperature nor decrease the pressure in the first hour because CHCl_3 will start to boil (boiling point at $61.2\text{ }^{\circ}\text{C}$) and the mixture will splash out of the mold. The vacuum oven is kept in these conditions until all gas bubbles are removed (\pm two hours). Next, the oven is cooled down at about 2 K min^{-1} to $25\text{ }^{\circ}\text{C}$, remaining under vacuum. During cooling, the forward Diels-Alder reaction takes place and the network is formed. The sheet is left at $25\text{ }^{\circ}\text{C}$ under vacuum for 24 hours to maximize the chloroform extraction. After this, the solid sheet can be demolded from the Telfon mold and the synthesis is completed.

Supporting Information 2: Fiber manufacturing via piston extrusion.

Ellen Roels, Seppe Terryn.

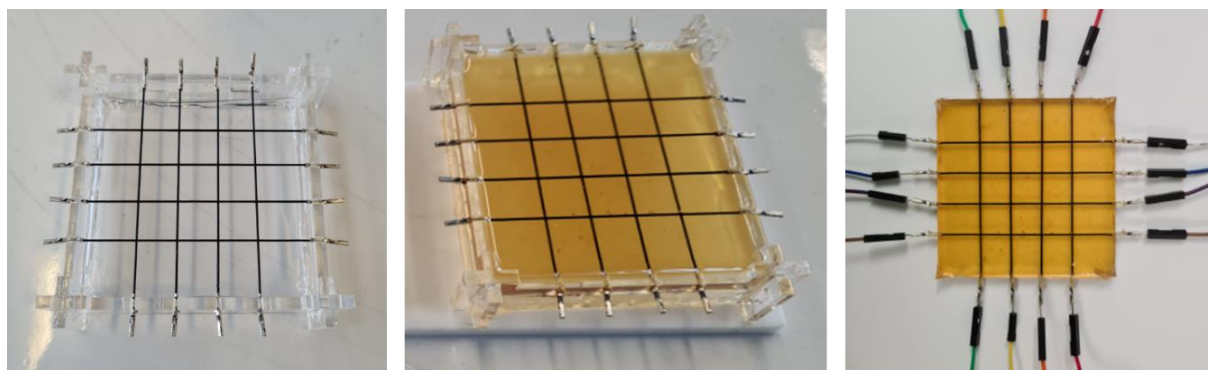
After solvent evaporation, the material was cut into pellets and extruded into a thin fiber using an in-house developed piston extruder. This device is designed for small-scale extrusion (± 5 g) and has an interchangeable nozzle, so different fiber diameters can be extruded when desired. For this work, we selected a nozzle size of 0.8 mm. The extruder is connected to a fixed bench vise that can be turned manually to extrude the fibers. The nozzle contains a cylindrical thermocouple and is enclosed by a 150W band heater. The temperature is controlled using a commercial PID-RS-S-48 ramp/soak controller. The fibers are extruded at 112°C, which is above the gel transition temperature T_{gel} of the composite. The piston provides the shear force that is required for the composite to flow. Upon exiting the nozzle, the composite gels into a solid polymer network and the fibers are left to rest for at least 24 hours to reach equilibrium before testing. Although the nozzle diameter is 0.8 mm, due to material stretching before it was collected, this results in a sensor fiber of around 0.5mm.



Supporting Information 3: Manufacturing of the electronic skin via casting.

Seppe Terryn.

The electronic skin is made through casting. First the fibers are cut to a length of 65 mm. Both ends are clamped in crimp connectors, which will form the connectors to jump wires at the ends of the electronic skin. Using these crimp connectors the fibers are straightened in a plexiglass mound. Four fibers are embedded straight in the x-directions with a distance of 11 mm between them and at a depth of 2.5 mm. The other fibers are embedded perpendicular to these, in the y-direction, also with a distance of 11 mm between them, but at a depth of 3.5 mm. Consequently, perpendicular fibers do not touch in the matrix. Next a mixture of BMI1400 and FT3000 is cast inside of the plexiglass mold. During the polymerization of the BMI1400-FT3000-r0.5, the material solidifies and fibers are embedded in the sheet, created insulated fibers in a grid composition inside the electronic skin. The manufacturing is completed upon leaving the part for 24 hours at 25°C.



Supporting Figures

David Hardman.

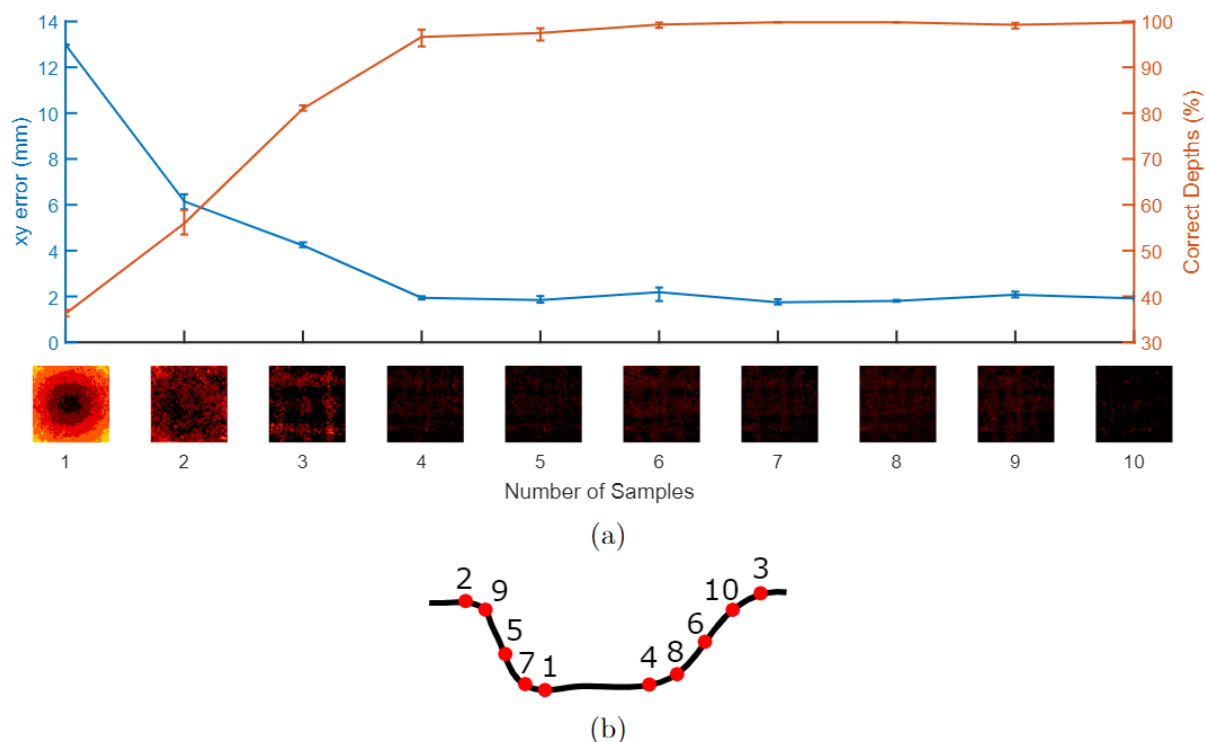


Figure S1: (a) Performances of ten networks trained, validated, and tested on the undamaged sensor. Each network uses the deep architecture presented in this work, with different sizes of input layer: ranging from 8 (1 sample from each sensor) to 80 (10 samples from each sensor). Values are evaluated using all 5000 collected data points. The order in which each of these samples is chosen is illustrated in (b). Improvements in performance saturate at approximately 5 samples per sensor.

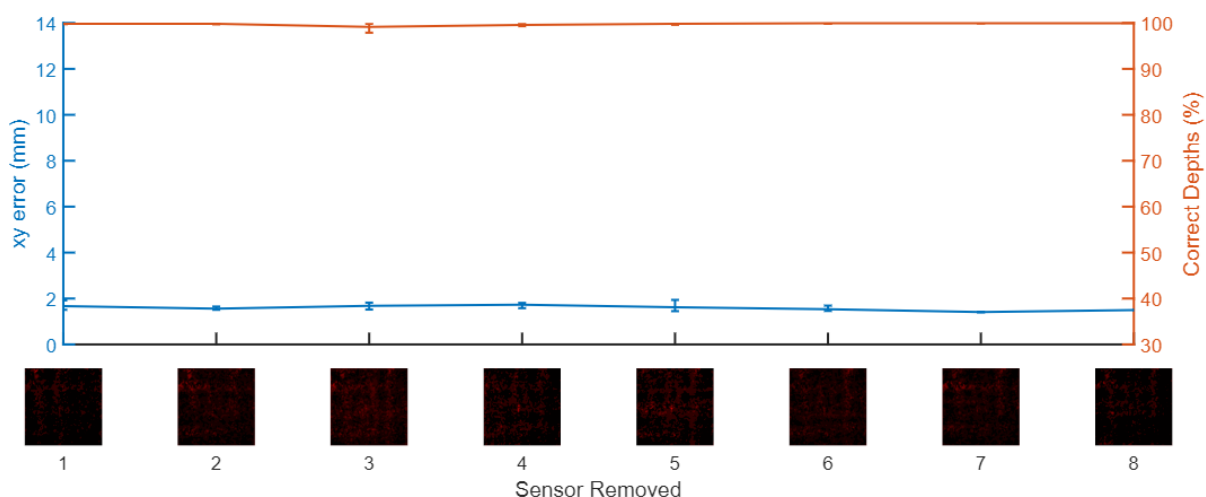
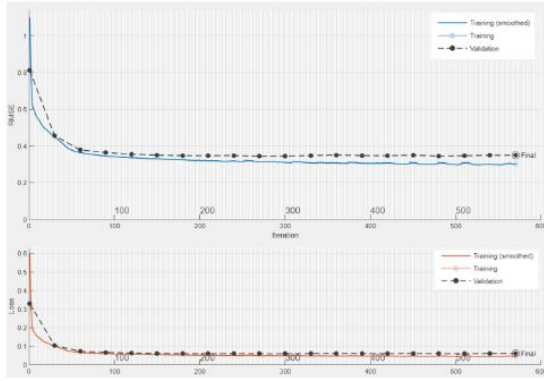
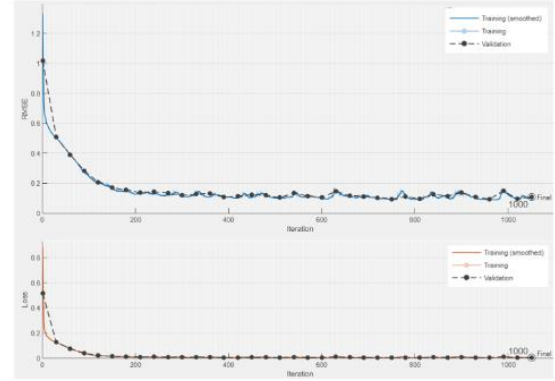


Figure S2: Performance of a 70-input network trained, validated, and tested on the skin after the first damage case. For each, one of the eight sensors' data is entirely removed. The uniform sensitivity maps, <2 mm localization, and ~100% depth predictions illustrate the redundancy

provided by multiple sensor responses, enabling the robustness of the skin to single damages. Values are evaluated using all 5000 collected data points.

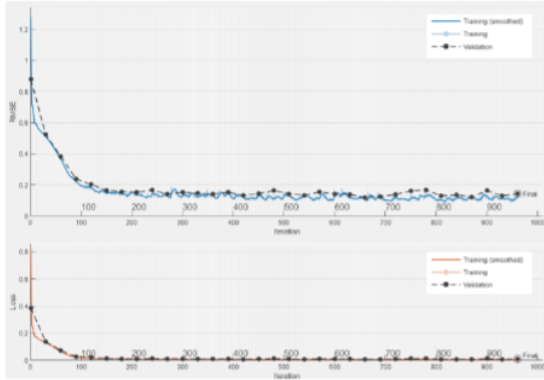


(a) 24-input

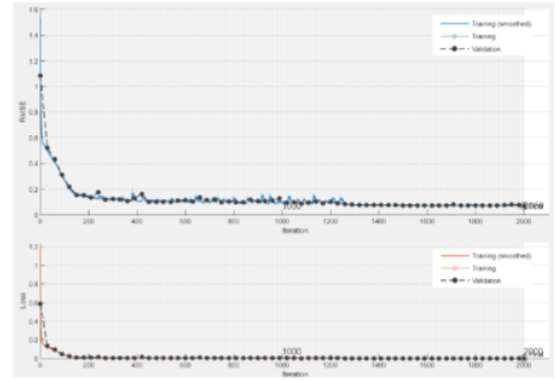


(b) 80-input

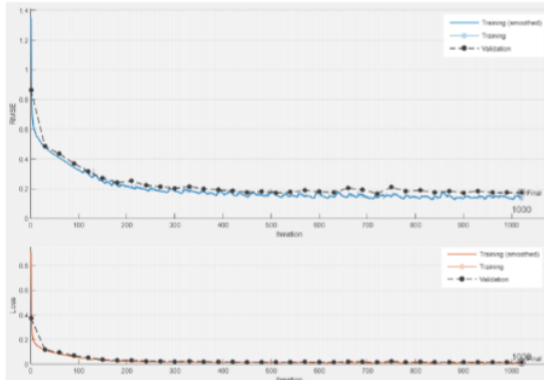
Figure S3: Initial training progress to the 5000 undamaged sensor responses (90:10% training:validation split), for networks with 24-neuron and 80-neuron input layers. Both meet the imposed validation criterion before the maximum number of iterations is reached.



(a) Healed Case 1



(b) Healed Case 2



(c) Healed Case 3

Figure S4: Training progresses of the 'no prior knowledge' (from scratch) networks to the three healed skin states. (a) & (c) meet the validation criterion, whilst (b) is halted after 2000 iterations.

Supporting Movies

David Hardman, Seppe Terryn, Thomas George Thuruthel.

Currently hosted [here](#).

Movie S1: A quickened video of the random probing process, in which x - y coordinates within the sensory grid are chosen at random and probed to a depth of 0.5, 1.0, or 1.5 mm. The timing of each press is standardized, and individual sensor responses are recorded in all cases.

Movie S2: Synchronizations of the voltage responses from each sensor's potential divider (0 → 5 V) during the three damage cases. In the first case, the matrix elasticity quickly restores contact once the scalpel is removed, returning the response to a mid-range value. This is not seen in the second or third damage cases: in the second, contact was quickly restored once probing began, whilst the third damage case had to be heated to initialize healing.

Movie S3: Responses of the three damaged skin states to probes along the lengths of the damaged sensor. This test was not explicitly performed for damage case 1, and has been artificially reconstructed from the 5000 random probes. As a result, this response shows more evidence of stochasticity and drift, but still illustrates the primary result: namely that contact is never lost for any sensor.

Movie S4: Responses of the three healed skin states to probes along the lengths of the damaged sensor. This test was not explicitly performed for damage case 1, and has been artificially reconstructed from the 5000 random probes.

Movie S5: Responses of the three damaged skin states to repeated probes at a sensory junction near the damaged area, showing initial drift followed by stabilization of the response. In the second case, this was the first test performed after damage; at the very start of the video, the first press is seen to cause recontact of the damage, which remains in place for all presses.

Movie S6: Responses of the three healed skin states to repeated probes at a sensory junction near the healed area, showing initial drift followed by stabilization of the response. Animation 3 is performed *after* that of Movie S4, such that resistances of some sensors are significantly increased.